

Simulations of Water Vapor and Clouds on Rapidly Rotating and Tidally Locked Planets: A 3D Model Intercomparison

Jun Yang^{1,2}, Jérémy Leconte³, Eric T. Wolf⁴, Timothy Merlis⁵, Daniel D.B. Koll⁶, François Forget⁷, and Dorian S. Abbot⁸

¹*Dept. of Atmospheric and Oceanic Sciences, School of Physics, Peking University, Beijing, 100871, China*

²*Previously at Dept. of the Geophysical Sciences, University of Chicago, Chicago, IL, 60637, USA*

³*Laboratoire d'astrophysique de Bordeaux, Univ. Bordeaux, CNRS, B18N, allée Groffroy Saint-Hilaire, Pessac, 33615, France*

⁴*Lab. for Atmospheric and Space Physics, University of Colorado in Boulder, Colorado, 80303, USA*

⁵*Dept. of Atmospheric and Oceanic Sciences at McGill University, Montréal, QC, H3A 0G4, Canada*

⁶*Dept. of Earth, Atmospheric and Planetary Sciences, MIT, Cambridge, MA, 02139, USA*

⁷*Lab. de Météorologie Dynamique, Institut Pierre Simon Laplace, CNRS, Paris, France*

⁸*Dept. of the Geophysical Sciences, University of Chicago, Chicago, IL, 60637, USA*

Correspondence: junyang@pku.edu.cn

ABSTRACT

Robustly modeling the inner edge of the habitable zone is essential for determining the most promising potentially habitable exoplanets for atmospheric characterization. Global Climate Models (GCMs) have become the standard tool for calculating this boundary, but divergent results have emerged among the various GCMs. In this study we perform an intercomparison of standard GCMs used in the field on a rapidly rotating planet receiving a G-star spectral energy distribution and on a tidally locked planet receiving an M-star spectral energy distribution. Experiments both with and without clouds are examined. We find relatively small difference (within 8 K) in global-mean surface temperature simulation among the models in the G-star case with clouds. In contrast, the global-mean surface temperature simulation in the M-star case is highly divergent (20-30 K). Moreover, even differences in the simulated surface temperature when clouds are turned off are significant. These differences are caused by differences in cloud simulation and/or radiative transfer, as well as complex interactions between atmospheric dynamics and these two processes. For example we find that

an increase in atmospheric absorption of shortwave radiation can lead to higher relative humidity at high altitudes globally and therefore a significant decrease in planetary radiation emitted to space. This study emphasizes the importance of basing conclusions about planetary climate on simulations from a variety of GCMs, and motivates the eventual comparison of GCM results with terrestrial exoplanet observations to improve their performance.

Subject headings: astrobiology — planets and satellites: atmospheres — planets and satellites: general — methods: numerical — radiative transfer

1. Introduction

The “habitable zone” is the circumstellar region where an Earth-like planet can support liquid water on its surface (Kasting et al. 1993; Kopparapu et al. 2013; Kasting et al. 2014), which is essential for Earth-like life. The habitable zone concept has received increasing attention in recent years as the number of potentially habitable extrasolar planets has increased and future NASA missions to characterize the atmospheres of potentially habitable extrasolar planets are being planned. This has led to the application of sophisticated three-dimensional (3D) GCMs, which are capable of modeling atmospheric dynamics, clouds, and water vapor distributions, to the problem (e.g., Merlis & Schneider 2010; Edson et al. 2011; Pierrehumbert 2011; Leconte et al. 2013a,b; Yang et al. 2013, 2014; Shields et al. 2013, 2014; Wolf & Toon 2014; Wang et al. 2014, 2016; Wolf & Toon 2015; Way et al. 2015, 2017; Godolt et al. 2015; Kopparapu et al. 2016; Popp et al. 2016; Carone et al. 2014, 2015, 2016, 2017; Turbet et al. 2016; Salameh et al. 2017; Wolf 2017; Wolf et al. 2017; Haqq-Misra et al. 2017; Boutle et al. 2017; Kopparapu et al. 2017; Lewis et al. 2018; Bin et al. 2018; Turbet et al. 2018).

The inner edge of the habitable zone is marked by either a massive increase in surface temperature as a result of a fundamental limit on infrared emission to space by an Earth-like planet, the “runaway greenhouse,” or the loss of a planet’s water through photodissociation and hydrodynamic escape due to high surface temperatures and a moist stratosphere, a “moist greenhouse” (Kasting 1988). Since modern Earth is relatively near the inner edge of the habitable zone (Kopparapu et al. 2013), aspects of these processes can be modeled using GCMs that were primarily designed to model the climate of modern and ancient Earth. In contrast, modeling the outer edge of the habitable zone requires accurate modeling of radiative transfer at high CO₂ concentrations, CO₂ clouds, and the dynamical effects of CO₂ condensation (Wordsworth et al. 2011; Wordsworth 2015; Turbet et al. 2016). As a result, more GCMs have been applied to the inner edge of the habitable zone, which has exposed

the dramatic impact of differences in model formulations on its position.

GCMs generally disagree on the position of the inner edge of the habitable zone both for planets orbiting cool M stars and Sun-like G stars. For example, for a tidally locked planet orbiting an M star, Kopparapu et al. (2017) found that for a stellar temperature of 3,400 K, updating the radiative scheme in the CAM4 GCM moved the inner edge of the habitable zone (runaway greenhouse) from 83 % above modern Earth’s solar constant to 39 % above it. Moreover, if we consider a planet with Earth’s rotation rate receiving the Sun’s spectral energy distribution, a runaway greenhouse occurs in the LMDG GCM when the solar constant is increased by 10 % above modern Earth’s value (Leconte et al. 2013b), but has not occurred when it is increased by 15 % in ECHAM6 (Popp et al. 2016) and by 21 % in CAM4_WOLF (Wolf & Toon 2015). These authors diagnosed differences in cloud simulation among their GCMs, but the lack of a uniform modeling framework made it impossible to firmly establish the cause of differences in cloud behavior, as well as whether variation in other processes might be important.

To clarify the situation, we organized a GCM intercomparison to investigate the causes of differences among GCMs that have been used to simulate the inner edge of the habitable zone in more detail. The participating GCMs are listed in Table 1. We started with a set of standardized one-dimensional radiative calculations with assumed vertical profiles of temperature and water vapor, and found that differences among the GCM radiative schemes in both longwave and shortwave are mainly due to differences in water vapor absorption (Yang et al. 2016). LMDG had the strongest greenhouse (longwave) effect and CAM3 had the weakest, with 17 W m^{-2} difference between them at a surface temperature of 320 K. In shortwave, CAM4_Wolf was the most absorptive¹ and CAM3 was the least, with a maximum top-of-atmosphere difference of $\sim 10 \text{ W m}^{-2}$ for a G star spectral energy distribution and $\sim 20 \text{ W m}^{-2}$ for a M star spectral energy distribution. The more sophisticated line-by-line radiative codes fell between these extremes in both longwave and shortwave. When we combined both longwave and shortwave fluxes to estimate the effective stellar flux of the inner edge of the habitable zone, we found a variation of about 10 % of modern Earth’s stellar flux among the GCMs due to differences in the treatment of water vapor radiative transfer alone.

The purpose of this paper is to extend the analysis of Yang et al. (2016) to the three-dimensional effects of GCMs. We have performed a set of standardized simulations for continent-free planets with (1) Earth’s rotation rate and the Sun’s spectral energy distribu-

¹E. T. Wolf has corrected this bias by improving the wavelength resolution of the stellar spectrum and absorption coefficients (e.g., Wolf 2017; Wolf et al. 2017).

tion, and (2) a tidally locked orbital configuration and an idealized M star spectral energy distribution (section 2). We will investigate model variation in these simulations, as well as analyze additional simulations designed to identify in more detail differences between CAM3, a cooler GCM, and LMDG, a warmer GCM (section 3). We conclude and discuss implications of this work in section 4.

2. Methods

The GCMs studied in this intercomparison and their resolutions are displayed in Table 1. CAM3 is CAM version 3, developed at NCAR (Collins et al. 2002). CAM4 is CAM version 4 (Neale et al. 2010) and CAM4_Wolf is CAM4 with a new radiative transfer module (<https://wiki.ucar.edu/display/etcam/Extraterrestrial+CAM>, see Wolf & Toon (2015)). AM2 is a 3D GCM developed at NOAA/GFDL (GFDL et al. 2004). LMDG is the 3D Laboratoire de Météorologie Dynamique (LMD) Generic Model, developed at LMD (Wordsworth et al. 2010a,b, 2011; Forget et al. 2013).

Table 1: List of the GCMs in this intercomparison. The horizontal resolution is given as latitude by longitude. We also performed some CAM3 simulations with $2.8^\circ \times 2.8^\circ$ horizontal resolution as well as CAM4 simulations with a $1.9^\circ \times 1.9^\circ$ horizontal resolution and with a finite volume dynamical core. Sensitivity tests using CAM3 with different model top pressures (0.9 and 0.1 hPa) showed that the model top pressure does not significantly influence the surface temperature.

GCM	Resolution	Levels	Top Pressure	Dynamical Core
CAM3	$3.75^\circ \times 3.75^\circ$	26	3.0 hPa	Spectral
CAM4	$3.75^\circ \times 3.75^\circ$	26	3.0 hPa	Spectral
CAM4_Wolf	$4.0^\circ \times 5.0^\circ$	45	0.2 hPa	Spectral
AM2	$2.0^\circ \times 2.0^\circ$	32	2.2 hPa	Finite-volume
LMDG	$2.8^\circ \times 2.8^\circ$	30	1.0 hPa	Finite-difference

We ran each GCM in a standard set of conditions. First, we ran them with a G star spectral energy distribution, a 24 hour rotation period, 365 Earth days per year, and both with and without clouds. Second, we ran them with an M star spectral energy distribution, tidally locked in a 1:1 synchronous rotation state, with a 60 day orbital and rotation period, and both with and without clouds. The G star spectral energy distribution was the default distribution in the GCM for the Sun. The M star spectral energy distribution was a black-body Planck distribution corresponding to a temperature of 3,400 K. AM2’s M star, with

clouds experiment did not converge due to an unresolved problem, so it is not listed in the following figures or tables.

We used a stellar flux of $1,360 \text{ W m}^{-2}$, zero obliquity, zero eccentricity and Earth’s radius and gravity for all simulations. We ran the models in aqua-planet mode (with no continents) with a 50-m deep mixed layer ocean and no ocean heat transport. The atmosphere was 1 bar of N_2 with 376 ppmv CO_2 and a variable amount of H_2O . We set CH_4 , N_2O , CFCs, O_3 , O_2 , and all aerosols to zero. We assumed no snow or sea ice, but allowed the sea surface temperature to drop below the freezing point. We set the surface albedo to 0.05 everywhere. We performed simulations both with clouds set to zero (more exactly, the radiative effects of clouds were turned off but cloud water and precipitation still formed) and with clouds calculated by the GCM cloud schemes. It should be noted here that because of the diversity of environments that have been modeled with LMDG, there are several possible cloud parametrizations available. Here we use the cloud parametrization and parameters from Charnay et al. (2013), where the cloud particle size distributions for both liquid droplets and ice particles are fixed. Another important point is how the total cloud fraction of an atmospheric column — the one that will be used in the radiative transfer calculation — is computed from the cloud fractions at all the modeled altitudes. In our baseline run (LMDG_max), we assume that clouds have a maximal recovery probability so that the total cloud fraction of the column is equal to the maximum cloud fraction at any altitude. We also present another set of simulations where we make the assumption that clouds at each level are uncorrelated, resulting in a random overlap (LMDG_random). We also performed more detailed simulations using CAM3 and LMDG run at a variety of stellar fluxes, and one example where we set water vapor to zero (a dry atmosphere) in both of these two models.

3. Results

3.1. G-star Planet GCM Comparison

Our first comparison involved planets in an orbital and rotational configuration similar to modern Earth’s, exposed to a G-star spectrum, with cloud radiative effects set to zero. As might be expected, differences in planetary albedo are small, within 0.01 (Table 2). This is consistent with the fact that the planetary albedos were fairly similar when the GCMs were run in 1D radiative-convective mode and forced with a G-star spectrum (see Fig. 7 in Yang et al. 2016). Part of the explanation for this may also be that the surface albedo is very low (0.05) in our experiments, so that 95% of light hitting the surface is absorbed, and differences among the models in shortwave absorption by atmospheric water vapor can have less effect on the planetary albedo. Yang et al. (2016) have already pointed out significant differences

in longwave radiative transfer that could result in different surface temperatures for a given shortwave heating, and this trend is confirmed here. Global-mean surface temperatures are within 1 K among CAM3, AM2, and CAM4_Wolf, but are 6 K lower in CAM4 and ≈ 12 K higher in LMDG, which was the model with the most pronounced greenhouse effect of water vapor (Fig. 3(a) in Yang et al. 2016).

It should not be too surprising to find such significant differences in temperature simulation of the group without clouds, especially between LMDG and the other GCMs. Turning off clouds in our aqua-planet configuration with a surface albedo of 0.05 results in a bond albedo of ≈ 0.10 - 0.11 , or equivalently a mean absorbed stellar flux of ≈ 303 - 306 W m^{-2} . This is just at the limit where some 1D saturated radiative-convective models are in a runaway greenhouse, such as LMDG and CAM4_Wolf, and others are not, such as CAM3 and CAM4 (see Fig. 3(a) of Yang et al. (2016)). Fortunately, atmospheric circulation-induced sub-saturation in the subtropics makes all the models in this experiment stable (Pierrehumbert 1995; Leconte et al. 2013a), but they are still functioning in a regime of high climate sensitivity due to the strong positive water vapor feedback. This means that small variations in shortwave absorption can lead to large variations in surface temperature.

Interestingly, both CAM4 and CAM4_Wolf exhibit spontaneous symmetry breaking in the cloud-free configuration, with a meridionally asymmetric climate resulting from symmetric boundary conditions (Fig. 1(a)). Sensitivity tests using CAM4_Wolf show that the hemisphere that contains the maximum in surface temperature depends on the initial conditions (figure not shown). The asymmetry results in a climate that is cooler than the other GCMs (Table 2), particularly in the case of CAM4, and foreshadows the important effects that differences in the simulation of atmospheric dynamics can produce in model climates in certain situations, which we will investigate further in section 3.3.

Including clouds cools all models (Table 2 and Fig. 1(b)), which is expected since clouds cool modern Earth. The global-mean net cloud radiative effect among the models varies greatly, from -32 to -55 W m^{-2} , mainly due to differences in cloud fraction and cloud water amount parameterizations (Fig. 2). The cloud radiative effect is more negative than its value on modern Earth (-20 W m^{-2} , Kiehl & Trenberth 1997), mainly because of the low surface albedo of a continent-free planet. Also, when clouds are included in the G-star spectrum calculations, meridional symmetry is restored to both CAM4 and CAM4_Wolf (Fig. 1(b)).

Interestingly, the global-mean surface temperature is more similar among the models when clouds are included than when they are not (Table 2). Part of the explanation for this may be that the models are cooler when clouds are included, and therefore farther from the runaway greenhouse where the climate sensitivity is high. Additionally, all of the models

Table 2: Global-mean climatic characteristics of the G-star spectrum GCM simulations.

Simulations	GCMs	T_S^a [K]	α_p^b [0-1]	SWCE ^c [Wm ⁻²]	LWCE ^d [Wm ⁻²]	NCE ^e [Wm ⁻²]	Cld ^f [%]	WVP ^g [kgm ⁻²]	CWP ^h [kgm ⁻²]
No Clouds	CAM3	307	0.10	—	—	—	—	100	—
	CAM4	301	0.10	—	—	—	—	62	—
	CAM4_Wolf	306	0.11	—	—	—	—	95	—
	AM2	307	0.10	—	—	—	—	99	—
	LMDG	319	0.11	—	—	—	—	178	—
With Clouds	CAM3	287	0.33	-78	39	-39	77	25	0.18
	CAM4	290	0.32	-73	41	-32	70	34	0.20
	CAM4_Wolf	289	0.33	-74	34	-40	70	30	0.17
	AM2	282	0.35	-83	35	-48	86	15	0.08
	LMDG_max	290	0.30	-64	30	-34	43	24	0.15
	LMDG_random	282	0.39	-94	39	-55	86	12	0.13

a. T_S : global-mean surface temperature

b. α_p : planetary albedo

c. SWCE: shortwave cloud radiative effect at the top of the model

d. LWCE: longwave cloud radiative effect at the top of the model

e. NCE: SWCE + LWCE

f. Cld: the total cloud coverage

g. WVP: the vertical-integrated water vapor content

h. CWP: the vertical-integrated cloud water (liquid plus ice) content

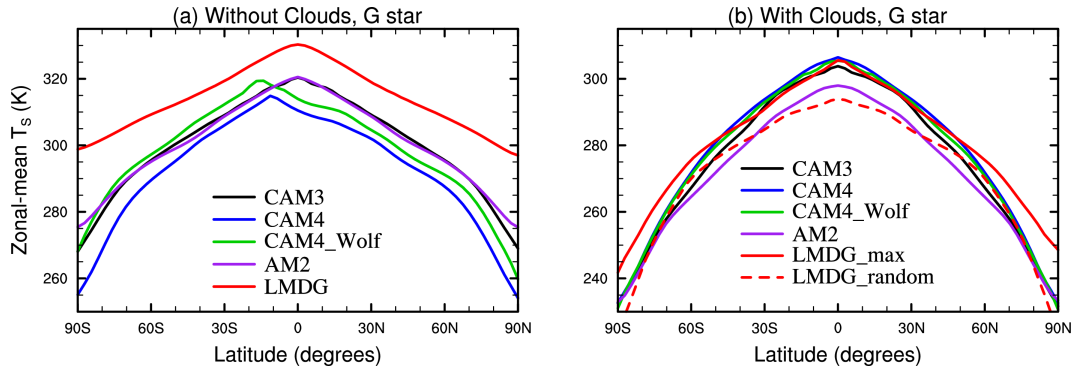


Fig. 1.— G star surface temperature: Zonal (East-West) mean surface temperature as a function of latitude for all GCMs both without clouds (a) and including clouds (b). The simulations assume a rapidly rotating aqua-planet with a G star stellar spectrum and a stellar flux of $1,360 \text{ W m}^{-2}$. LMDG_max assumes maximum overlap between different types of clouds at each altitude while LMDG_random employs a random overlap. Note the different y axis ranges between (a) and (b).

have been tuned to reproduce the surface temperature of modern Earth, which is close to the regime simulated here. It may be that the cloud parameterizations are tuned to compensate for differences in clear sky radiative transfer among the models.

It is important to note, however, that AM2 and LMDG_random are both 5–8 K colder than the other models (Table 2). Given that AM2 produced very similar surface temperatures to CAM3 in the simulations without clouds, we can attribute the difference in simulations with clouds to differences in cloud parametrization: The lower temperature is due to a stronger negative cloud radiative effect (-48 W m^{-2}), resulting in a higher planetary albedo. In fact, the cloud radiative effect at the top of the model is correlated with surface temperature in all the experiments, with a more negative cloud radiative effect associated with a lower global-mean surface temperature (Table 2). Similarly, the difference between LMDG_max and LMDG_random is entirely due to clouds, and shows that in this configuration switching from one extreme assumption on the cloud overlap to the other can have a 8 K effect on the global-mean surface temperature.

Spatial patterns of cloud fraction as well as cloud water amount are similar among the models, but the magnitudes have very large differences. All models show broadly similar patterns of cloud fraction, with pronounced Intertropical Convergence Zones (ITCZs) and relatively low-level clouds at mid and high latitudes (Fig. 2(a-f)). The cloud fraction is generally higher in AM2 than in the CAM models. This, in combination with potential

microphysical differences (such as cloud particle size), is likely why AM2 produces a more negative cloud radiative effect and lower surface temperatures, although its cloud water amount is the lowest among the models (Fig. 2(g–l)). CAM3 is slightly cloudier than CAM4 and CAM4_Wolf, as was found by Wolf & Toon (2015), which likely causes its slightly lower global-mean surface temperature. Cloud fraction in LMDG_max is less than that in LMDG_random while the cloud water amount is similar between the two versions of LMDG, so that clouds have a larger cooling effect in LMDG_random, -55 versus -34 W m^{-2} (Table 2 and Fig. 2(e–f, k–l)).

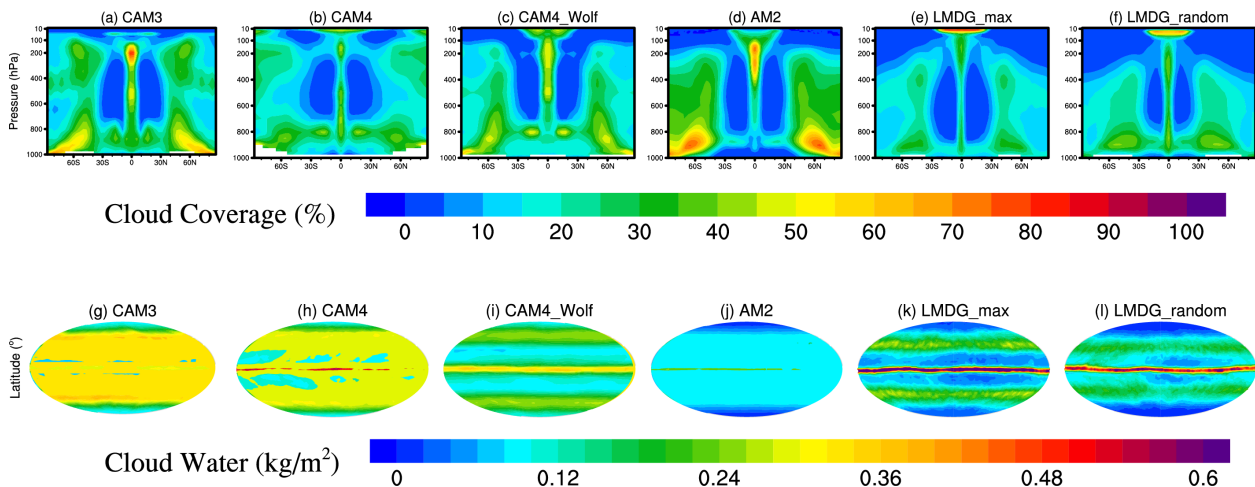


Fig. 2.— G star clouds: Upper panels: Contour plots of zonal (East-West) mean cloud fraction as a function of latitude and pressure (vertical) and lower panels: Vertically integrated cloud water amount (including both liquid and ice phases), for all GCMs. The simulations assume a rapidly rotating aqua-planet with a G star stellar spectrum and a stellar flux of $1,360$ W m^{-2} .

3.2. M-star Planet GCM Comparison

When we ran the GCMs in tidally locked configuration with an M-star spectrum, they produced larger differences than in the G-star case, even without clouds (Fig. 3(a)). CAM3 produced the coolest climate, which is consistent with the fact that it has the weakest greenhouse effect in 1D radiative-transfer mode (Yang et al. 2016). CAM4_Wolf is warmer than CAM3, CAM4 and AM2; a major cause of this is likely that the greenhouse effect of water vapor in CAM4_Wolf is the strongest among the four models (Yang et al. 2016). The CAM models and AM2 show a range of behavior, with differences in surface temperature among

models particularly pronounced on the night side. This is likely due to the large changes in surface temperature possible if the strength of the night-side temperature inversion changes. This effect is leveraged by increases in the radiative time scale and atmospheric heat transport (Koll & Abbot 2016), due to larger water vapor concentration in warmer simulations. Parameterization of boundary layer turbulence could also influence the inversion strength and the night-side surface temperature. Moreover, the water vapor feedback acts to amplify the differences among models (Fig. 4(a)). LMDG obtains the highest global-mean surface temperature in the no-cloud experiment, 14–28 K larger than other models (Table 3). As in the G-star, no-cloud experiment, although LMDG does not enter the runaway greenhouse at this insolation ($1,360 \text{ W m}^{-2}$) it is very close to the runaway greenhouse. The absorbed stellar energy of the system in this experiment is 326 W m^{-2} in global mean (the planetary albedo is 0.04)². Near or in the runaway greenhouse state, outgoing longwave radiation at the top of the atmosphere is insensitive to surface temperature and therefore a large increase in the surface temperature is required to balance even a very small increase in stellar radiation absorption (Pierrehumbert 2010).

Note, a robust feature of these simulations is that, despite the lower albedo, all models are cooler in the tidally locked setup than in the rapidly rotating setup. This is mainly due to the radiator fin effect of the permanent night side of a tidally locked orbit, which is relatively drier and can therefore emit longwave radiation to space more easily (Pierrehumbert 1995; Yang & Abbot 2014).

With clouds included, the various versions of CAM yield surprisingly similar surface temperatures (Fig. 3(b)), especially given the variation in M-star spectral energy distribution stellar absorption in 1D radiative-transfer mode (Yang et al. 2016), although CAM4-Wolf does have a global-mean surface temperature about 5–6 K higher (Table 3). However, the global-mean surface temperature of LMDG is 10–26 K higher than those in CAM models. The remarkable divergence among models emphasizes the fact that we should not over-interpret the results of any single model when simulating exoplanet climates.

The most striking feature of the GCM cloud simulation in the M-star, tidally locked case (Fig. 5) is that all models confirm previous work (Yang et al. 2013; Way et al. 2015;

²Note that the runaway greenhouse limit depends on the orbital configuration of the planet. For example, in the lower resolution LMG simulations described in Section 3.3, the absorbed stellar energy in the last converged solution is $\simeq 323 \text{ W m}^{-2}$ in the tidally locked, no-cloud configuration, but it is $\simeq 315 \text{ W m}^{-2}$ in the rapidly rotating, no-cloud configuration (Fig. 6). The higher value in the tidally locked configuration is mainly due to the radiator fin effect of the permanent night side of a tidally locked orbit, which is relatively drier and can therefore emit longwave radiation to space more easily (Pierrehumbert 1995; Yang & Abbot 2014).

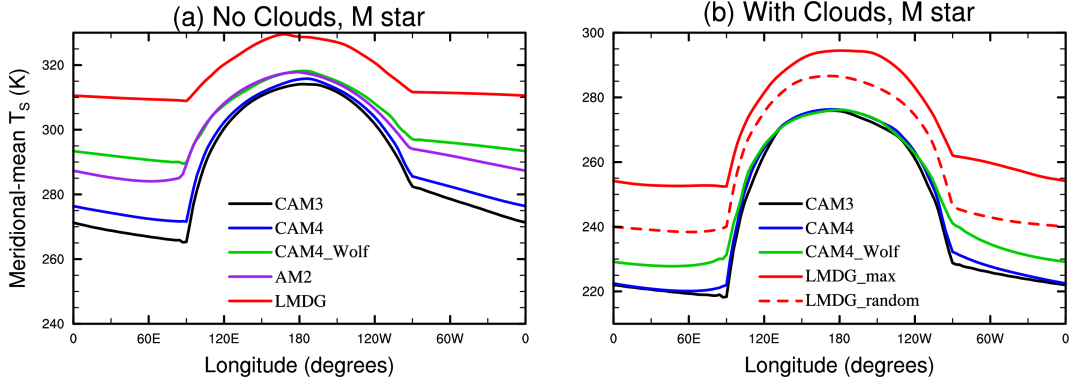


Fig. 3.— M star surface temperature: Meridional (North-South) mean surface temperature as a function of longitude for GCMs both without clouds ((a), CAM3, CAM4, CAM4_Wolf, AM2, and LMDG) and including clouds ((b), CAM3, CAM4, CAM4_Wolf, LMDG_max, and LMDG_random). The configuration assumes a tidally locked aqua-planet with an M star stellar spectrum and a stellar flux of $1,360 \text{ W m}^{-2}$. The substellar point is at 180° longitude. Note the different y axis ranges between (a) and (b).

Table 3: Global-mean climatic characteristics of the M-star spectrum GCM simulations. For the notes of different variables, please see Table 2. An insolation of $1,360 \text{ W m}^{-2}$ is close to the runaway greenhouse of LMDG when cloud radiative effects are turned off, explaining the high temperature of the model. The with-clouds case of AM2 met one unresolved problem, so that the experiment is not listed in the table.

Simulations	GCMs	T_S [K]	α_p [0-1]	SWCE [Wm^{-2}]	LWCE [Wm^{-2}]	NCE [Wm^{-2}]	Cld [%]	WVP [kgm^{-2}]	CWP [kgm^{-2}]
No Clouds	CAM3	288	0.04	—	—	—	—	84	—
	CAM4	291	0.04	—	—	—	—	106	—
	CAM4_Wolf	302	0.04	—	—	—	—	155	—
	AM2	299	0.04	—	—	—	—	136	—
	LMDG	316	0.04	—	—	—	—	268	—
With Clouds	CAM3	246	0.46	-138	17	-121	97	7	0.15
	CAM4	247	0.46	-140	21	-119	98	9	0.17
	CAM4_Wolf	252	0.44	-131	19	-112	98	13	0.19
	LMDG_max	272	0.30	-82	20	-62	34	41	0.15
	LMDG_random	262	0.38	-108	22	-86	81	22	0.11

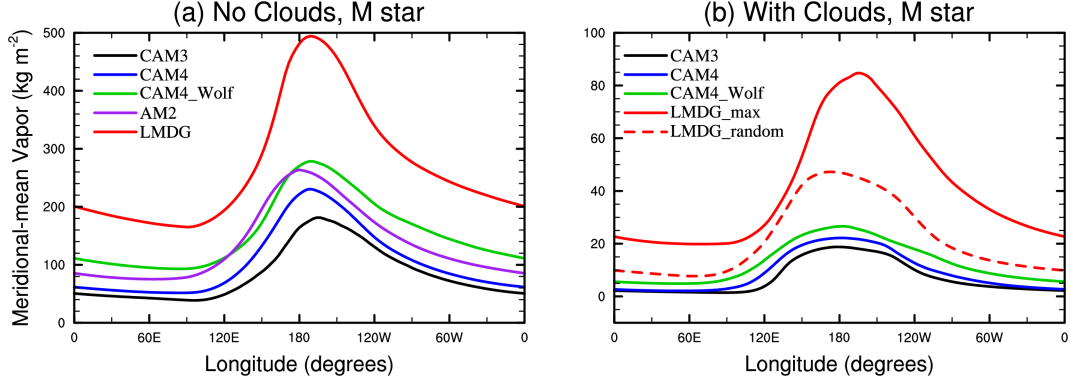


Fig. 4.— M star water vapor content: Meridional (North-South) mean vertically integrated water vapor content in the atmosphere as a function of longitude for GCMs both without clouds ((a), CAM3, CAM4, CAM4_Wolf, AM2, and LMDG) and including clouds ((b), CAM3, CAM4, CAM4_Wolf, LMDG_max, and LMDG_random). The configuration assumes a tidally locked aqua-planet with an M star stellar spectrum and a stellar flux of $1,360 \text{ W m}^{-2}$. Note the different y axis ranges between (a) and (b).

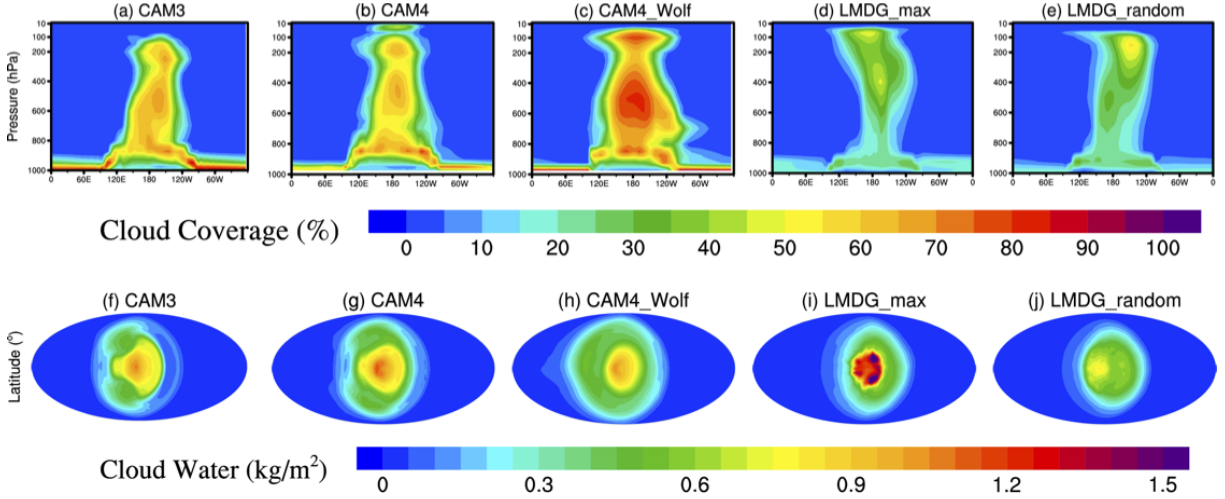


Fig. 5.— M star clouds: Upper panels: Contour plots of meridional (North-South) mean cloud fraction as a function of longitude and pressure (vertical), and lower panels: Vertically integrated cloud water amount (including both liquid and ice phases), for GCMs CAM3, CAM4, CAM4_Wolf, LMDG_max, and LMDG_random. The configuration assumes a tidally locked aqua-planet with an M star stellar spectrum and a stellar flux of $1,360 \text{ W m}^{-2}$.

Kopparapu et al. 2016; Salameh et al. 2017) predicting deep convective clouds at the substellar point. We find that LMDG has relatively low cloud fractions that are somewhat weighted toward high altitude, optically thin clouds (Fig. 5(a–e)). This contributes significantly to the fact that LMDG produces much higher surface temperatures than the CAM models. The planetary albedos in LMDG_max and LMDG_random are 0.30 and 0.38, respectively, about 0.16 and 0.08 lower than those in CAM3 (Table 3). LMDG_max has a much lower cloud fraction but higher cloud water amount than LMDG_random (Fig. 5(d–e, i–j)), such that LMDG_max has a weaker net cloud radiative effect, -62 versus -86 W m^{-2} , and a warmer surface, 272 versus 262 K in global mean. Most models produce boundary layer clouds on the night side, but these have very little radiative effect. Again, the water vapor feedback is important for enhancing differences among models (Fig. 4(b)).

3.3. Explaining Differences Between CAM3 and LMDG

In order to investigate the mechanistic causes of differences among GCMs in more detail, we performed additional simulations and analyses of CAM3, a relatively cool GCM, and LMDG, a relatively warm GCM. Fig. 6 shows a comparison of the global mean surface temperature in CAM3 and LMDG as a function of both incoming stellar flux and absorbed stellar flux in both tidally locked and rapidly rotating aqua-planet configurations forced by both G-star and M-star spectral energy distributions. Clouds are set to zero in all of these simulations.

Both models are warmer for a given stellar flux when forced by an M-star spectral energy distribution because water vapor absorbs longer wavelengths of light better. Under the same incoming stellar flux, the global-mean surface temperature in the rapidly rotating case is higher than that in the tidally locked case. This is mainly due to the cooling effect of the radiator fin of the permanent night side on tidally locked planet (Pierrehumbert 1995; Yang & Abbot 2014). When we plot as a function of absorbed stellar flux, the difference between G-star and M-star surface temperatures within a model is greatly reduced. Plotted in this way though, a cold offset of CAM3 relative to LMDG appears, and the offset becomes larger with increasing stellar flux. There are several processes that may cause the differences between CAM3 and LMDG, including radiative transfer, atmospheric dynamics, and differences in the water vapor distribution due to differences in convection parameterizations and dynamical processes. We will investigate these below, focusing our attention on the tidally locked case around an M star, where differences between the two models are largest.

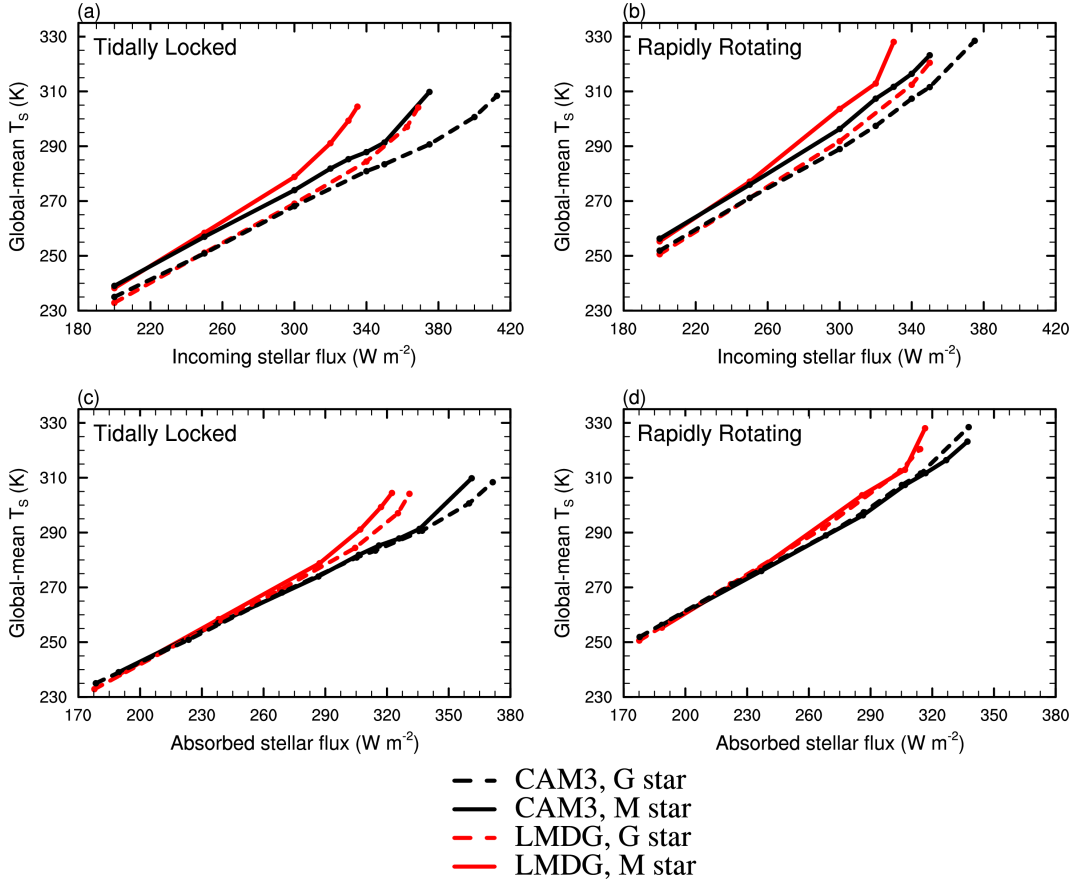


Fig. 6.— Global-mean surface temperature as a function of global-mean incoming stellar flux (a, b) and absorbed stellar flux (c, d) for CAM3 (black lines) and LMDG (red lines) when the GCMs are run in a tidally locked aqua-planet configuration (a, c) and a rapidly rotating aqua-planet configuration (b, d) with a G star stellar spectrum (dashed lines) and with an M star stellar spectrum (solid lines). Clouds are turned off in all these simulations, and the surface albedo is 0.05 everywhere. Note that the maximum stellar fluxes at the substellar point of the tidally locked experiments in (a) and (c) are $1,650 W m^{-2}$ (CAM3, G star), $1,500 W m^{-2}$ (CAM3, M star), $1,475 W m^{-2}$ (LMDG, G star) and $1,340 W m^{-2}$ (LMDG, M star), and of the rapidly rotating experiments in (b) and (d) are $1,500 W m^{-2}$ (CAM3, G star), $1,400 W m^{-2}$ (CAM3, M star), $1,400 W m^{-2}$ (LMDG, G star) and $1,320 W m^{-2}$ (LMDG, M star). A further increase of the stellar flux in LMDG will push LMDG into a runaway greenhouse state or CAM3 to blow up. Note: To speed up computations, we decreased the resolution of LMDG to $11.25^\circ \times 5.625^\circ$ in the simulations for this figure. Although this will not affect the trends discussed here, it may affect the exact location of the runaway greenhouse limit of the model.

3.3.1. *Clear-sky Radiative Transfer*

When forced by the same 1D temperature and water vapor profiles, CAM3 absorbs less radiation in both infrared and visible wavelengths than LMDG, i.e., CAM3 has a weaker greenhouse effect and smaller shortwave energy absorption (Yang et al. 2016). These differences result from LMDG using an updated HITRAN database, HITRAN2008 versus HITRAN2000 in CAM3 (Yang et al. 2016). HITRAN2008 has many more absorption lines and stronger absorption cross sections in many wavelengths than HITRAN2000 (Supplementary Fig. 3 in Goldblatt et al. (2013)). Moreover, there are 36 stellar spectrum intervals in LMDG and only 7 in CAM3 (Yang et al. 2016). The higher spectral resolution in LMDG allows it to accurately resolve the individual absorption and window wavelengths separately. We confirm these differences here by inputting the simulated 3D temperature and water vapor profiles from LMDG into CAM3’s radiative transfer module (Fig. 7). We find that the outgoing longwave radiation using CAM3’s radiation is higher than LMDG’s by 3.8 W m^{-2} in the global mean and the absorbed shortwave radiation by the atmosphere using CAM3’s radiation is lower than LMDG’s by 11.7 W m^{-2} in the global mean. Both of these effects lead to a cooler climate in CAM3. Consistent with this finding, Kopparapu et al. (2017) showed that accounting for these updated line lists and continuum absorption coefficients reduces the stellar flux limit for the runaway greenhouse.

3.3.2. *Dry Dynamical Core*

To test for dynamical differences between the two models, we performed tidally locked simulations with an M-star spectral energy distribution, no clouds, and with atmospheric water vapor mixing ratio set to 10^{-6} everywhere, which is the minimum vapor concentration covered by the radiative transfer correlated- K tables in LMDG. The surface temperature simulation was nearly identical between the two models in this case (Fig. 8), in fact, LMDG was actually slightly cooler than CAM3. This is in striking contrast to the same simulation performed with water vapor and clouds, where LMDG produced a climate much warmer than CAM3 (Table 3). This test shows that dry dynamics alone do not contribute significantly to differences in the simulation of climate in LMDG and CAM3.

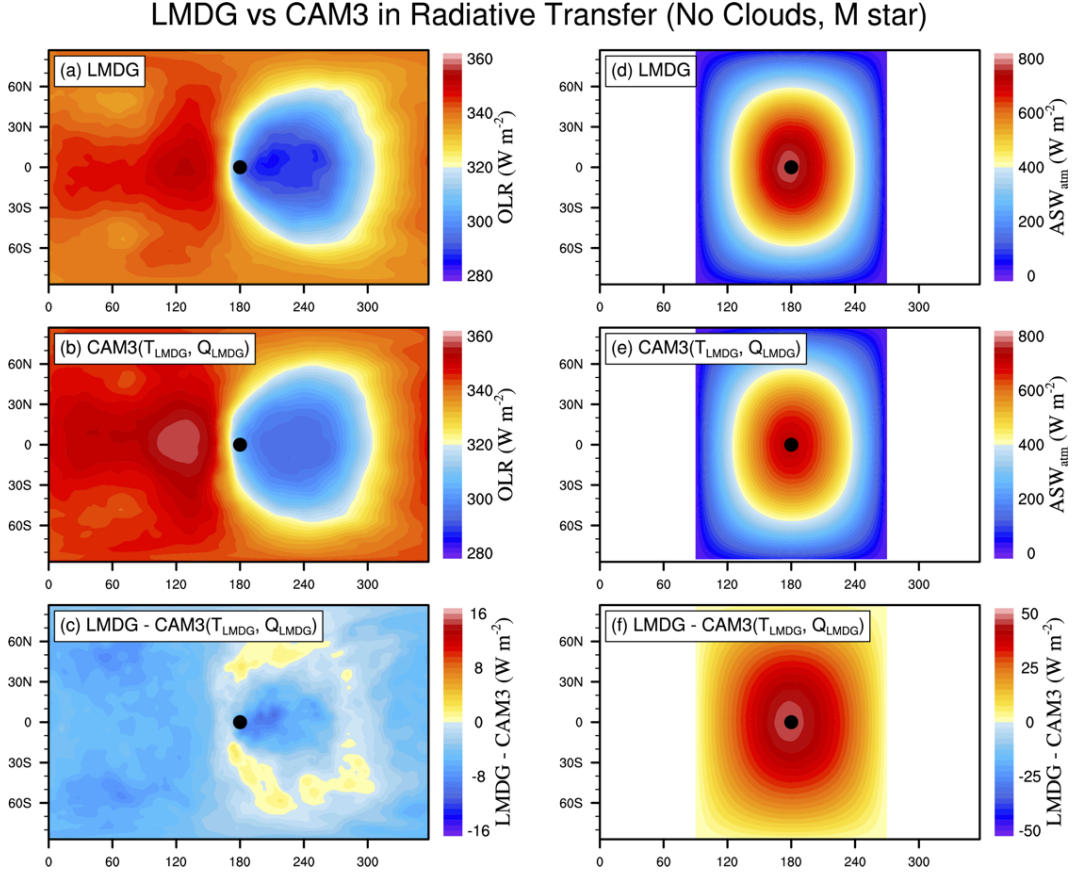


Fig. 7.— Cloud-free radiative transfer in LMDG and CAM3: Outgoing longwave radiation (OLR) at the top of the model (left column) and absorbed shortwave flux by the atmosphere (ASW_{atm}) for LMDG and for CAM3 forced by the same temperature and water vapor profiles from LMDG. (a) OLR in LMDG, (b) OLR in CAM3, and (c) the difference: LMDG – CAM3. (d) ASW_{atm} in LMDG, (e) ASW_{atm} in CAM3, and (f) the difference: LMDG – CAM3. The black dot is the substellar point. The global-mean value is -3.8 W m^{-2} in (c) and 11.7 W m^{-2} in (f).

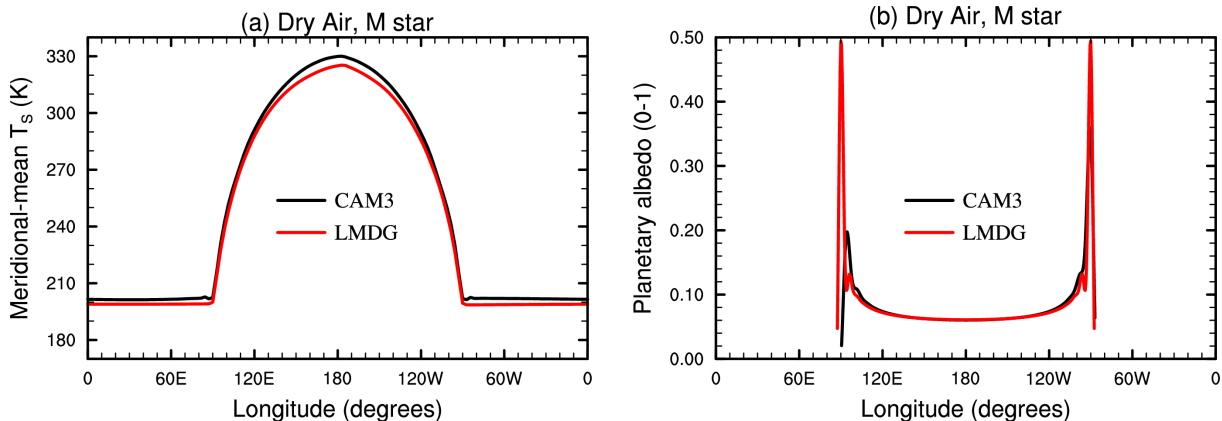


Fig. 8.— Dry atmosphere simulations: Meridional (North-South) mean surface temperature (a) and planetary albedo (b) as a function of longitude for both CAM3 and LMDG assuming a nearly dry atmosphere on a tidally locked planet with a stellar flux of $1,360 \text{ W m}^{-2}$. The water vapor mixing ratio is set to 10^{-6} everywhere, which is the minimum vapor concentration allowed in the radiative transfer correlated- K tables of LMDG.

3.3.3. Relative Humidity

We next turn our attention to the simulation of relative humidity (RH), which is defined as the percentage of water vapor mixing ratio³ relative to the saturation water vapor mixing ratio (Wallace & Hobbs 2016; Abbot 2018) and is a critical term for inferring habitability (Pierrehumbert 1995; Leconte et al. 2013a; Pierrehumbert & Ding 2016) that can be affected by both radiative transfer and atmospheric dynamics. Relative humidity is higher in LMDG than in CAM3 at high altitude around the planet, both with and without clouds (Fig. 9). High-altitude water vapor is particularly important because it increases the optical thickness in a cold region of the atmosphere, causing strong greenhouse warming. The fact that the high-altitude relative humidity is much higher in LMDG than in CAM3 is likely one of the causes of the much higher surface temperature in LMDG.

Atmospheric relative humidity is determined by many processes, including large-scale atmospheric circulation, eddies, and small-scale processes such as convection, entrainment, detrainment, re-evaporation of rain droplets, and diffusion (Pierrehumbert et al. 2007; Sher-

³An alternative definition is ratio of the vapour pressure to the saturation vapor pressure (such as Vallis (2017)). The American Meteorological Society (AMS) uses the vapor pressure to define RH while the World Meteorological Organization (WMO) used the mixing ratio to define RH (glossary.ametsoc.org). The differences between these two definitions are very small when the water vapor is dilute.

wood et al. 2010; Wright et al. 2010). Here, we can identify two factors that likely make LMDG moister. The first is that LMDG uses a forced convective adjustment (Manabe & Wetherald 1967) to calculate the atmospheric lapse rate, whereas CAM3 determines the atmospheric lapse rate prognostically based on complex moist processes (Wolf & Toon 2015). This difference can have a big impact on moisture distributions, as Wolf & Toon (2015) found when they compared LMDG and CAM4_Wolf, which determines the lapse rate in a similar way to CAM3. Specifically, they showed that in hot climates, even under the same global-mean surface temperature, LMDG’s upper atmosphere is always much moister than CAM4_Wolf’s. Next we suggest a second reason LMDG may be moister: differences in shortwave absorption.

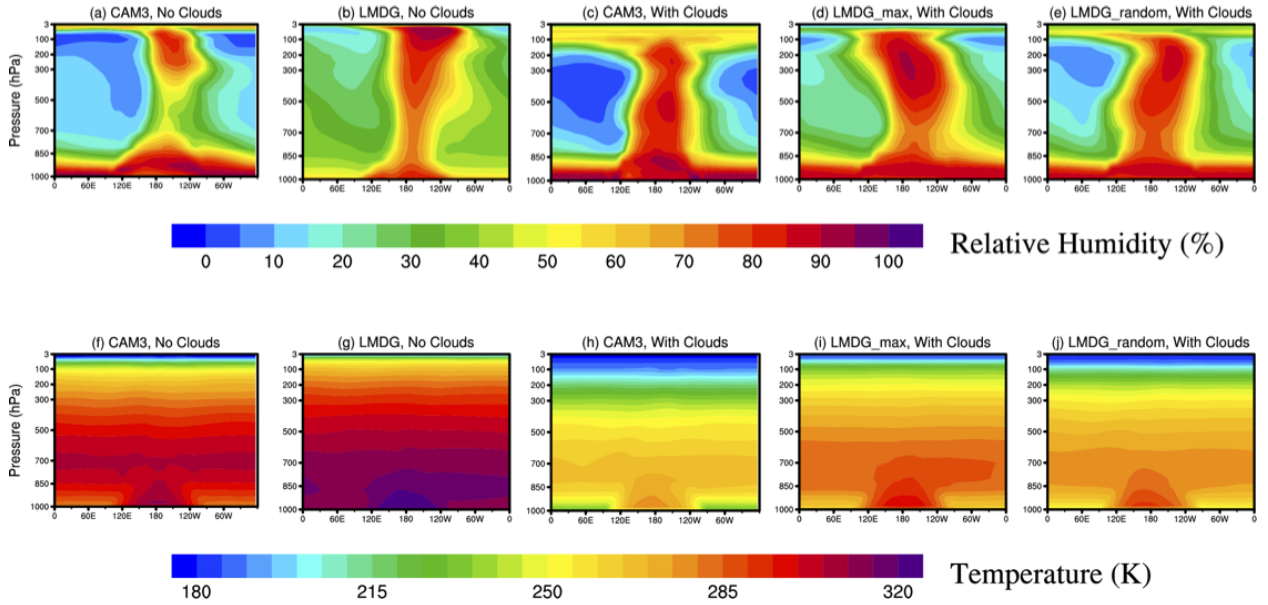


Fig. 9.— M star relative humidity and air temperature: Contour plots of meridional (North-South) mean relative humidity (upper panels) and air temperature (lower panels) as a function of longitude and pressure (vertical) for CAM3 and LMDG. The simulations are for a tidally locked aqua-planet with an M star stellar spectrum and a stellar flux of $1,360 \text{ W m}^{-2}$. Simulations both without clouds (a, b, f, g) and with clouds (c–e, h–j) are plotted.

A major difference between CAM3 and LMDG is that absorption of stellar radiation by water vapor is significantly higher in LMDG than in CAM3 (section 3.3.1). When we artificially increased the shortwave water vapor absorption coefficient in CAM3, we found that this significantly increased the high-altitude relative humidity and surface temperature (Fig. 10). When we doubled the absorption coefficient by water vapor, the shortwave heating rate of the atmosphere in CAM3 is close to that in LMDG (Fig. 11), the global-mean

surface temperature increases by 0.9 K, and the night-side surface temperature increases by 2.5 K⁴. In CAM4_Wolf, we find the same phenomenon: When the shortwave water vapor absorption coefficient is decreased, the high-altitude relative humidity decreases and the surface cools (Fig. 12). To understand this, we built a last saturation model for water vapor (Pierrehumbert et al. 2007) in which we trace air parcels and approximate their specific humidity as its value the last time the parcel was saturated (see Appendix A). Model resolution and numerical diffusion limit the accuracy of this method, but we are able to broadly reproduce the high-altitude relative humidity.

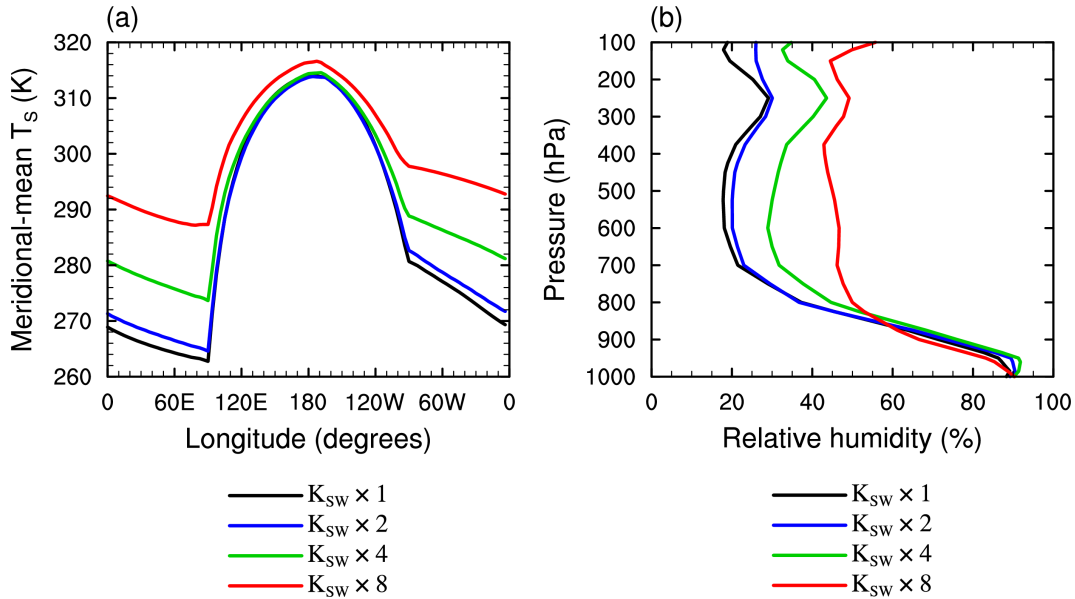


Fig. 10.— Varying the shortwave absorption coefficient of water vapor (K_{H_2O}) in CAM3: Meridional (North-South) mean surface temperature as a function of longitude (left) and global mean vertical profiles of relative humidity (right) for the simulations with K_{H_2O} increased by a multiple of 1, 2, 4, or 8. The simulations are for a tidally locked aqua-planet with an M star stellar spectrum, a stellar flux of $1,292 \text{ W m}^{-2}$, and without clouds. The surface albedo is set to zero everywhere, so that the planetary albedo is close to zero in all of these cases (not shown). Note that the 4 and 8 times absorption coefficients are unrealistic. Increasing the absorption coefficients by about twice in CAM3 is able to approximately match the shortwave heating rates in LMDG (see Fig. 11 below).

⁴Although seemingly small, this effect would be further amplified by the strong positive water vapor radiative feedback if another source of heating—an increase in longwave absorption for example—were to be added.

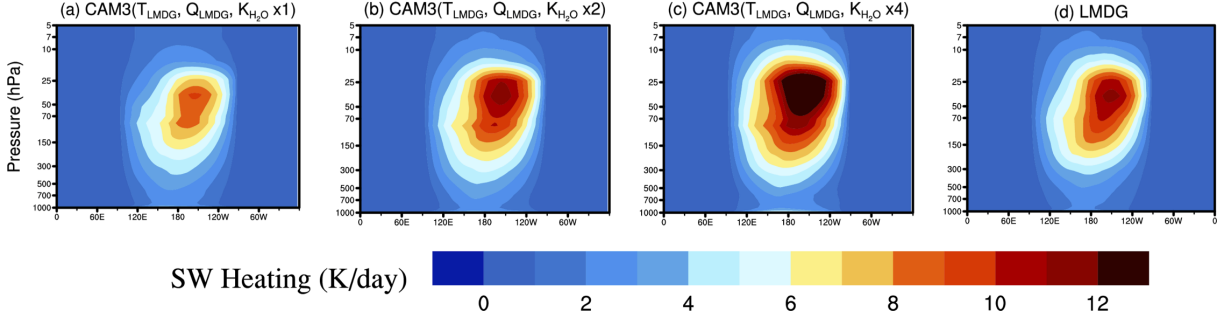


Fig. 11.— Meridional (North-South) mean shortwave heating rate: CAM3 versus LMDG. (a) Using CAM3’s default shortwave absorption coefficient of water vapor (K_{H_2O}), (b) doubling the values of K_{H_2O} , (c) quadrupling the values of K_{H_2O} , and (d) LMDG. In the calculations, CAM3’s radiative transfer module is forced by temperature and water vapor profiles from LMDG. The calculations are for a tidally locked aqua-planet with an M star stellar spectrum, a stellar flux of $1,360 \text{ W m}^{-2}$, and without cloud radiative effects.

As air parcels rise in convection in the substellar region, they tend to experience detrainment and convective outflow at some pressure associated with an anvil cloud. This will mark the point of last saturation, as the air is subsequently advected away from the substellar point and descends to higher pressures as it cools radiatively and heats adiabatically. As shown in Fig. 13, for a given pressure in the descending region (P_2), the relative humidity (RH_2) is determined by the temperature and the air pressure at the last saturation point (T_1 and P_1), and can be approximately written as,

$$RH_2 = 100 \frac{e(T_2)}{e_{sat}(T_2)} \frac{P_2 - e_{sat}(T_2)}{P_2 - e(T_2)} \approx 100 \frac{e(T_2)}{e_{sat}(T_2)} \approx 100 \left(\frac{e_{sat}(T_1)}{e_{sat}(T_2)} \right) \times \left(\frac{P_2}{P_1} \right), \quad (1)$$

where e_{sat} is the saturation vapor pressure, e is the vapor pressure, and we have assumed the vapor pressure is much less than the air pressure at and after the last saturation. It has previously been shown that the Fixed Anvil Temperature hypothesis (Hartmann & Larson 2002; Kuang & Hartmann 2007; Thompson et al. 2016) holds fairly well for convection near the substellar point of tidally locked simulations in CAM3 (Yang & Abbot 2014). This implies that the temperature of the point of last saturation (T_1) and the corresponding saturation vapor pressure ($e_{sat}(T_1)$) should stay roughly constant⁵ as we increase the shortwave water

⁵The FAT hypothesis denotes that the temperature at the detrainment level of tropical convective anvil clouds is nearly constant during climate change. The underlying mechanism is that energy balance in the tropical troposphere is primarily between convective heating by latent heat release in regions of deep convection and radiative cooling by longwave emission to space in clear-sky regions with large-scale subsidence.

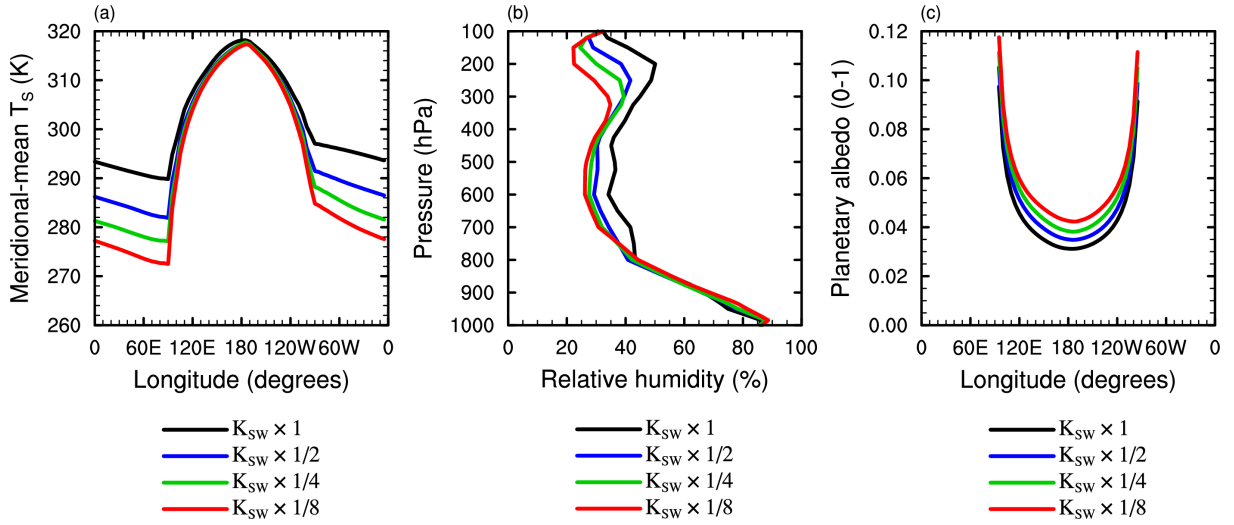


Fig. 12.— Varying the shortwave absorption coefficient of water vapor (K_{H_2O}) in CAM4.Wolf: Meridional (North-South) mean surface temperature (a) and planetary albedo (c) as a function of longitude, and global-mean vertical profiles of relative humidity (b) for the simulations with K_{H_2O} decreased by a multiple of 1, 1/2, 1/4, or 1/8. The simulations are for a tidally locked aqua-planet with an M star stellar spectrum, a stellar flux of $1,360 \text{ W m}^{-2}$ and without clouds. The global-mean surface temperatures are 302, 297, 295 and 292 K, and the planetary albedos are 0.044, 0.049, 0.053 and 0.057, respectively. The surface albedo is 0.05 everywhere. The tiny changes in planetary albedo are not enough to explain the changes in surface temperature.

vapor absorption coefficient, but the pressure (P_1) should decrease due to surface warming and an increase in the altitude of the anvil cloud. This is exactly what we see in CAM3 (Fig. 14). Since the temperature at last saturation (T_1) does not change much as the short-wave water vapor absorption coefficient is increased, the saturation vapor pressure ($e_{sat}(T_1)$) does not change much. But the air pressure (P_1) decreases, so the specific humidity at last saturation must increase. Another way to explain this is that there is the same amount of water vapor (same temperature), but much less dry air (lower pressure), so the water vapor specific humidity increases. This means the relative humidity will be higher all along the air parcel’s subsequent trajectory, and explains why increasing the shortwave water vapor absorption coefficient increases the high-altitude relative humidity throughout the planet.

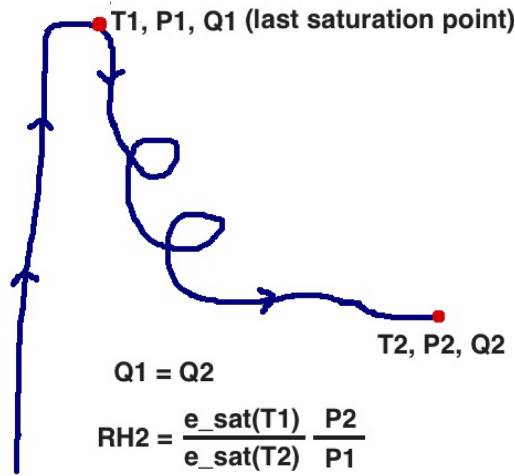


Fig. 13.— Schematic illustration of the last saturation model for an air parcel. Specific humidity is conserved after the time of last saturation. T represents the air parcel’s temperature, P its pressure, and Q its specific humidity.

In addition to the shortwave water vapor absorption coefficient, we have tested the sensitivity of CAM3 to a number of other parameters. These include: numerical momentum

Because of this, the detrainment level of anvil clouds should be located at the altitude where the clear-sky radiative cooling diminishes rapidly. The clear-sky radiative cooling rate in the upper troposphere is primarily determined by water vapor emission. The temperature at which the saturation water vapor pressure becomes small enough that water vapor emission is ineffective is constrained by local air temperature because of the Clausius–Clapeyron relationship. Therefore, the temperature at the top of anvil clouds should be nearly independent of surface temperature. For the simulations without clouds in our study, we turn off the cloud radiative effects but cloud formation, latent heat release, precipitation, and clear-sky radiative transfer still exist, so that the FAT hypothesis works in our simulations.

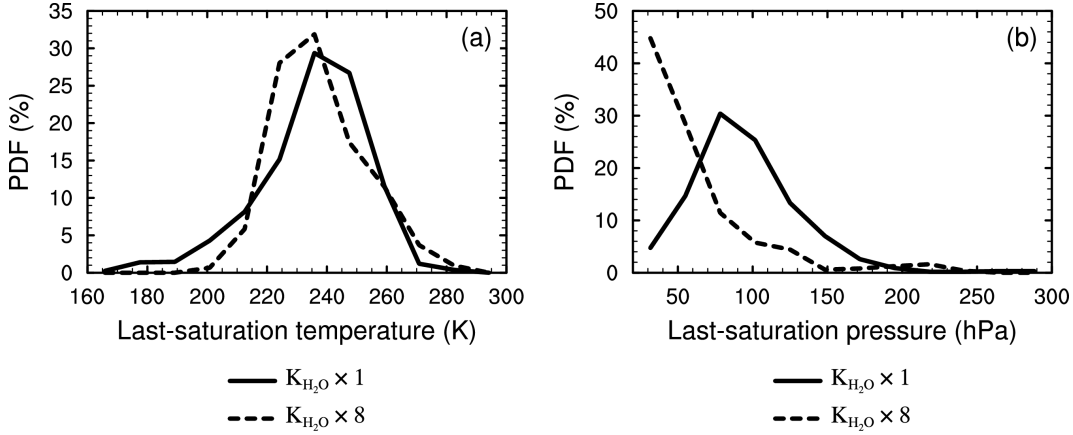


Fig. 14.— Probability distribution functions (PDFs) of the last saturation temperature ((a), T_1 in Fig. 13) and pressure ((b), P_1 in Fig. 13) for CAM3 run with normal shortwave water vapor absorption coefficient K_{H_2O} (solid) and with eight times K_{H_2O} (dashed).

diffusion near the top of the model (0.1 or 100 times of the default value), surface momentum transfer coefficient (0.1 or 10 times of the default value), sensible and latent heat exchange coefficients (0.5 or 2 times of the default value), deep and shallow convection relaxation timescales (from 0.1 hr to 16 hrs), deep and shallow convection precipitation efficiencies (0.1 or 10 times of the default value), deep convection downdraft mass flux factor (from 0 to 0.7), relative humidity limit for large-scale condensation (from 50% to 99.9%), convective and large-scale precipitation evaporation efficiencies (0.1 or 10 times of the default value), and the critical Richardson number for planetary boundary mixing (from 0.1 to 1). In all of these tests, the global-mean surface temperature in the cloud-free, M-star, tidally locked configuration is within the range of 286–294 K, indicating that varying one single parameter can induce a global-mean surface temperature difference within 8 K. More work would be required to test the effect of varying two or more parameters simultaneously.

3.3.4. Summary

To summarize, there are a number of differences between LMDG and CAM3 that lead to CAM3 simulating a much colder climate for tidally locked, M-star planets. Differences in the models’ radiative schemes lead to LMDG absorbing more stellar radiation and emitting less planetary radiation to space. The interplay between atmospheric dynamics and cloud parameterization leads to a higher cloud fraction and cloud optical thickness at the substellar point in CAM3, causing significant cooling. Finally, moist processes and the interplay

between the absorption of stellar radiation and atmospheric dynamics leads to higher relative humidity at high altitudes in LMDG, and therefore lower planetary thermal radiation to space, causing significant warming of LMDG.

4. Conclusion and Discussion

In this paper we have performed an intercomparison of the 3D global climate models CAM3, CAM4, CAM4-Wolf, AM2, and LMDG both with and without clouds. Our conclusions are as follows:

1. When run with clouds for rapidly rotating planets receiving a G-star spectral energy distribution and a stellar flux of $1,360 \text{ W m}^{-2}$, the models produce global mean surface temperatures within 8 K. Small differences in cloud parameterization assumptions can lead to this level of variation, as shown by the LMD_max and LMD_random simulations.
2. When run with clouds for tidally locked planets receiving an M-star spectral energy distribution and a stellar flux of $1,360 \text{ W m}^{-2}$, the GCM's behavior is much more divergent (up to 26 K in global-mean surface temperature). LMDG_max is much warmer than the other models. Clouds are an important part of the reason for this behavior, but large differences among the models with clouds set to zero demonstrate that model divergence is also due to clear-sky radiative effects of water vapor, as well as the interaction of radiation with atmospheric dynamics.
3. We implemented a last saturation model for relative humidity and used it to show that a larger shortwave water vapor absorption in GCM leads not only to direct warming by decreasing the planetary albedo, but also to indirect warming by increasing the high-altitude relative humidity around the planet and therefore decreasing planetary radiation emitted to space (increasing the greenhouse effect).

Besides of the differences in surface temperature, air temperature, and relative humidity between the models, there are also significant differences in stratospheric water vapor concentration (Fig. 15), which influences the onset of the moist greenhouse state and the location of the inner edge of the habitable zone. From this figure, one could find that the stratospheric water vapor concentration is not directly connected to surface temperature, and it is more directly determined by air temperatures at high altitudes. The surface temperature difference among the models in the M-star, tidally locked experiments is larger than in the G-star, rapidly rotating experiments, but the stratospheric water vapor difference above 30

hPa is smaller in the former group of experiments. The strength of stratospheric circulation, such as the Brewer-Dobson circulation on Earth, can also influence the stratospheric water vapor (Holton et al. 1995; Danielsen 1993; Fueglistaler & Haynes 2005; Roms & Kuang 2009). Future work is required to analyze the differences in stratospheric circulation and troposphere–stratosphere water vapor exchange between the models.

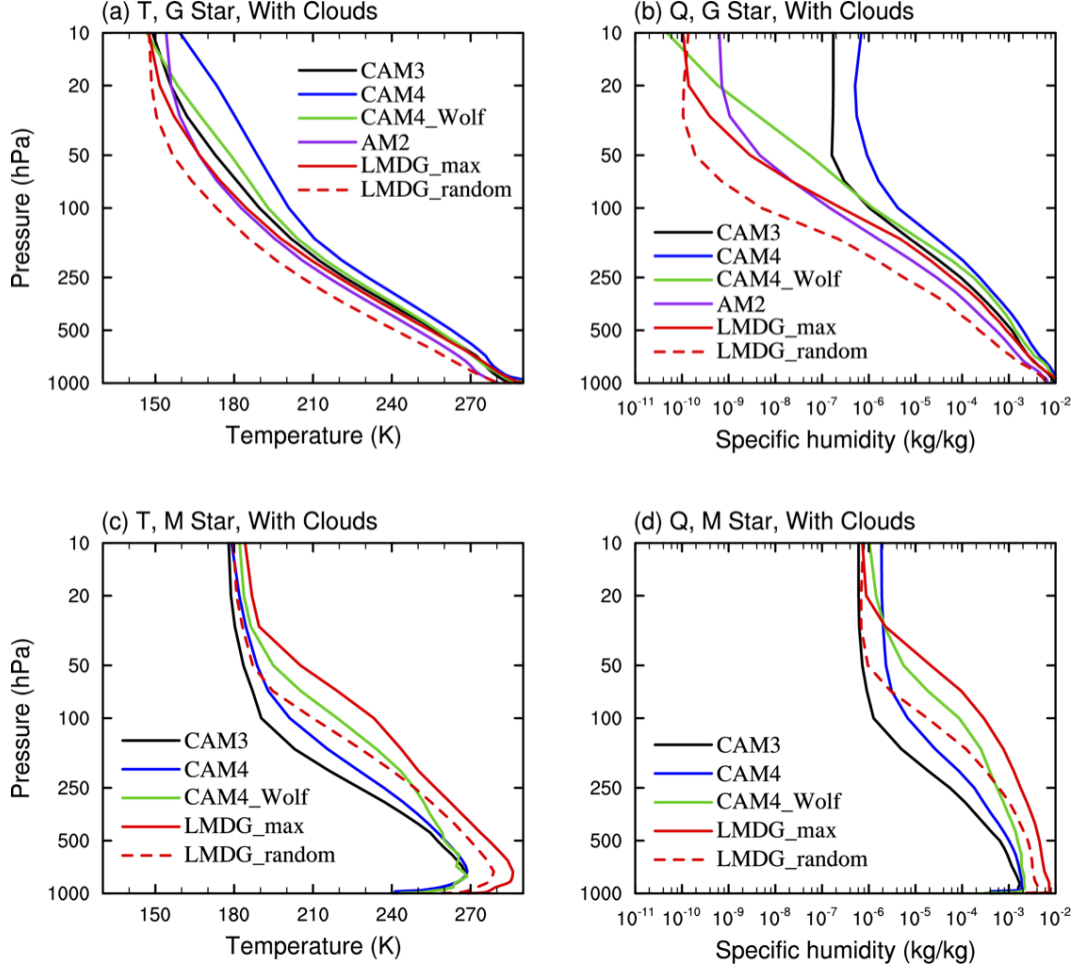


Fig. 15.— Global-mean temperature profiles (a & c) and specific humidity profiles (b & d). (a & b) The simulations assume a rapidly rotating aqua-planet with a G star stellar spectrum, a stellar flux of $1,360 \text{ W m}^{-2}$, and clouds. (c & d) The simulations assume a tidally locked aqua-planet with an M star stellar spectrum, a stellar flux of $1,360 \text{ W m}^{-2}$, and clouds. No ozone is included in all of the simulations.

Our results are useful in explaining the differences between models those have been employed to examine the location of the inner edge of the habitable zone, such as why

LMDG enters a runaway greenhouse state in a lower stellar radiation than that in the CAM models (Leconte et al. 2013b; Yang et al. 2013; Wolf & Toon 2015). Moreover, our results suggest that future work in developing exoplanet climate models should focus on improving the radiative transfer of water vapor in both longwave and shortwave and updating the cloud parameterization. In the present GCMs, the accuracy in shortwave radiative transfer is lower than that in longwave radiative transfer. Before direct atmospheric observations of exoplanets, laboratory cloud experiments and high-resolution cloud resolving models could be employed to investigate the clouds under different planetary parameters and the results could be used to improve the cloud parameterization in GCMs. When interpreting the differences and similarities among the models considered here, it is important to emphasize that agreement among some or most of the GCMs does not imply that the climates they simulate are correct. This is particularly true for the CAM models, which share a similar heritage, and therefore share many similar or identical subroutines. Determining which GCMs are the most accurate requires detailed comparison with observations from Earth, other solar system planets, and eventually observations of exoplanets. We should also remember that a GCM might perform better in one context and worse in another.

Since we performed the simulations for this intercomparison, three new planetary GCMs have been developed: Resolving Orbital and Climate Keys of Earth and Extraterrestrial Environments with Dynamics (ROCKE-3D) (Way et al. 2017), the Met Office Unified Model (UM) (Boutle et al. 2017), and Isca (Vallis et al. 2018) as well as others. Readers should be aware of these models and future intercomparison efforts should include them.

Acknowledgments: We acknowledge support from NASA grant number NNX16AR85G, which is part of the “Habitable Worlds” program and from the NASA Astrobiology Institutes Virtual Planetary Laboratory, which is supported by NASA under cooperative agreement NNH05ZDA001C. J.Y. acknowledges support from the National Science Foundation of China (NSFC) grants 41861124002, 41675071, 41606060, and 41761144072. J.L. acknowledges that this project has received funding from the European Research Council (ERC) under the European Unions Horizon 2020 research and innovation programme (grant agreement number 679030/WHIPLASH). We are grateful to Junyan Xiong for his help in drawing Figures 13 and 16. This work was completed in part with resources provided by the University of Chicago Research Computing Center.

A. Last Saturation Model

This appendix briefly describes the last saturation model we built for relative humidity in the CAM3 GCM based on the method of Pierrehumbert et al. (2007). The model works by tracking an air parcel as it moves around the planet and assuming that its specific humidity is conserved after it reaches saturation for the last time (Fig. 13). This model does not include processes such as numerical diffusion that can occur in the GCM. In a tidally locked planet, last saturation generally occurs when convective ascent at the substellar point ceases. The air parcel then flows away from the substellar point and descends as it cools radiatively and heats adiabatically. We can see these processes occurring in Fig. 16, which shows the trajectory of an example parcel and the relative humidity we can infer for it using the last saturation method. The last saturation model is able to reproduce the broad pattern of high-altitude relative humidity as simulated by CAM3 (Fig. 17). In particular, the model reproduces the low relative humidity on the night side, with approximately the correct magnitude. As would be expected for a model without numerical diffusion, the relative humidity field from the last saturation model is somewhat more noisy than that from CAM3.

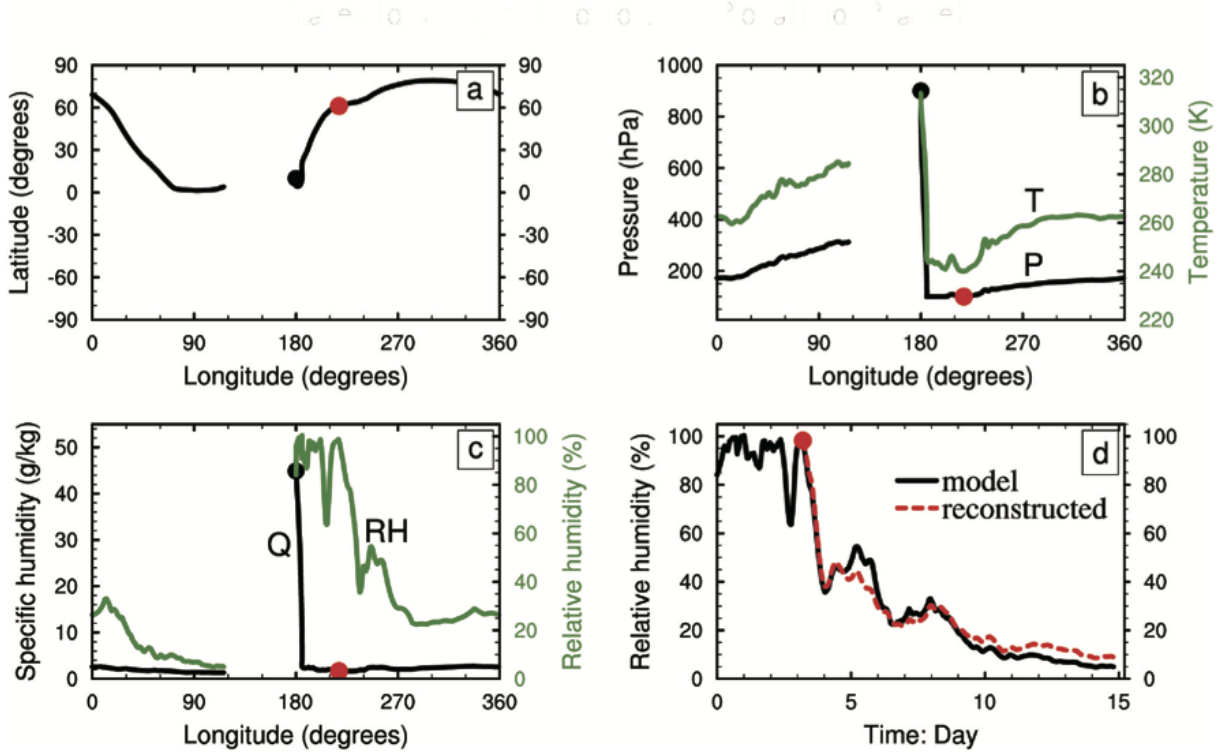


Fig. 16.— This is an example of the trajectory of an air parcel that we trace using the last saturation model. The black dot in all panels shows where we begin to trace the parcel and the red dot shows where it last reaches saturation. Panel (a) shows the latitude and longitude of the parcel as it rises near the substellar point and is advected away from the substellar point at altitude. Panel (b) shows the air pressure and temperature of the parcel as a function of longitude as it makes its voyage. Last saturation is achieved at the coldest air temperature reached. Panel (c) shows the specific and relative humidities of the parcel as a function of longitude. Panel (d) shows the GCM relative humidity (black line) and the relative humidity reconstructed from the last saturation model (red line) as a function of time. The red dot has a relative humidity of 90 % rather than 100 % (same as Wright et al. (2010)); this is because of the large grid size of the GCM (about 300 km) which means much of the air would saturate when the grid-mean relative humidity is 90 %. The substellar point is at 0° latitude and 180° longitude.

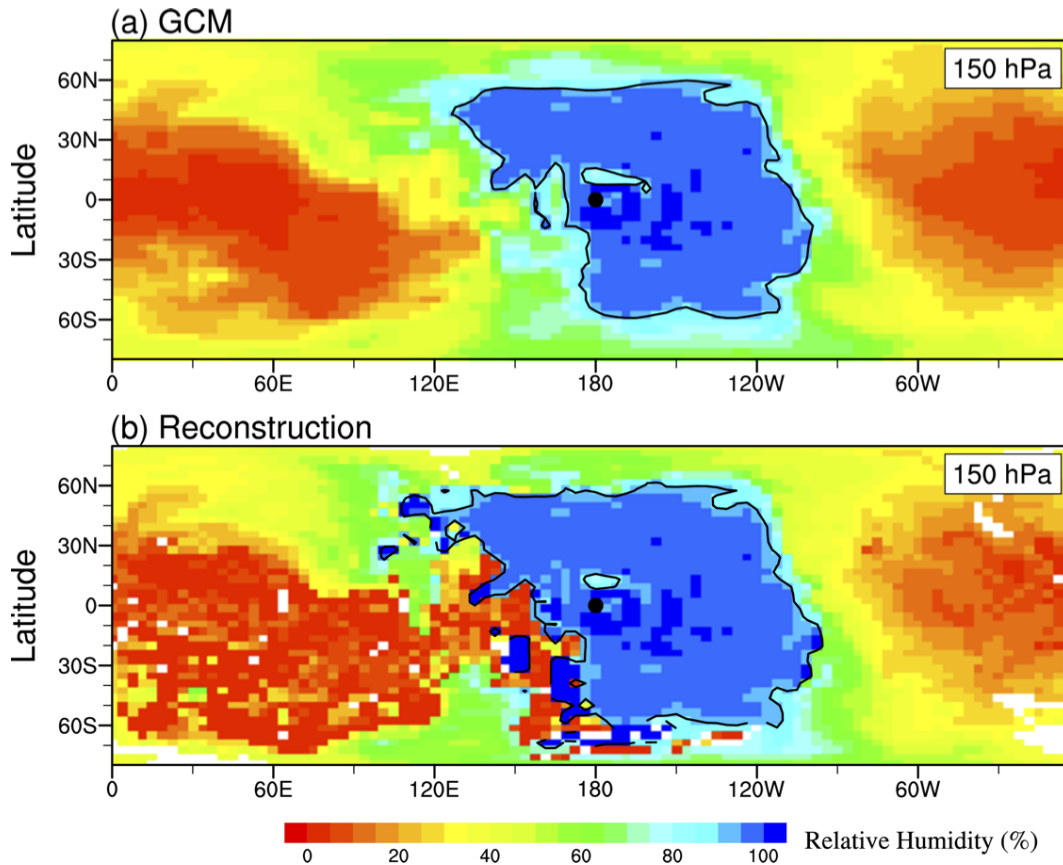


Fig. 17.— Here the high-altitude (150 hPa) relative humidity from GCM (a) is compared to the reconstructed relative humidity using the last saturation model (b) in a model snapshot. The white spots in the last saturation model represent areas that no air parcel we traced ended up at this particular time snapshot. The model is run in tidally locked aqua-planet configuration and forced with an M-star spectral energy distribution. The black dot is the substellar point, and the black line is the contour of a relative humidity of 90%.

REFERENCES

- Abbot, D. S. 2018, <https://arxiv.org/abs/1806.04481>, pp. 182
- Bin, J., Tian, F., & Liu, L. 2018, *EPSL*, 492, 121
- Boutle, I. A., Mayne, N. J., Drummond, B., Manners, J., Goyal, J., Lambert, F. H., Acreman, D. M., & Earnshaw, P. D. 2017, *Astronomy & Astrophysics*, 601, A120
- Carone, L., Keppens, R., & Decin, L. 2014, *Monthly Notices of the Royal Astronomical Society*, 445, 930
- . 2015, *Monthly Notices of the Royal Astronomical Society*, 453, 2412
- . 2016, *Monthly Notices of the Royal Astronomical Society*, 461, 1981
- Carone, L., Keppens, R., Decin, L., & Henning, T. 2017, *Monthly Notices of the Royal Astronomical Society*, 473, 4672
- Charnay, B., Forget, F., Wordsworth, R., Lecointe, J., Millour, E., Codron, F., & Spiga, A. 2013, *JGR: Atmospheres*, 118
- Collins, W. D., et al. 2002, Description of the NCAR Community Atmosphere Model (CAM3), <http://www.cesm.ucar.edu/models/atm-cam/#documentation> pp. 189
- Danielsen, E. F. 1993, *JGR*, 98, 8665
- Edson, A., Lee, S., Bannon, P., Kasting, J. F., & Pollard, D. 2011, *Icarus*, 212, 1, DOI:10.1016/j.icarus.2010.11.023
- Forget, F., Wordsworth, R. D., Millour, E., Madeleine, J.-B., & Charnay, B. 2013, *Icarus*, 222, 81
- Fueglistaler, S., & Haynes, P. H. 2005, *JGR-Atmos*, 110, D24108, doi:10.1029/2005JD006019
- GFDL et al. 2004, *Journal of Climate*, 17, 4641
- Godolt, M., et al. 2015, *Planetary and Space Science*, 111, 62
- Goldblatt, C., Robinson, T. D., Zahnle, K. J., & Crisp, D. 2013, *Nature Geoscience*, 6, 661
- Haqq-Misra, J., Wolf, E., Joshi, M., Zhang, X., Kopparapu, R. K., et al. 2017, *The Astrophysical Journal*, 852, 1
- Hartmann, D. L., & Larson, K. 2002, *Geophysical Research Letters*, 29

- Holton, J. R., Haynes, P. H., McIntyre, M. E., Douglass, A. R., Rood, R. B., & Pfister, L. 1995, *Rev. Geophys.*, 33, 403
- Kasting, J. F. 1988, *Icarus*, 74, 472
- Kasting, J. F., Kopparapu, R. K., Ramirez, R. M., & Harman, C. E. 2014, *Proceedings of the National Academy of Sciences*, 111, 12641
- Kasting, J. F., Whitmire, D. P., & Reynolds, R. T. 1993, *Icarus*, 101, 108
- Kiehl, J. T., & Trenberth, K. E. 1997, *Bulletin of the American Meteorological Society*, 78, 197
- Koll, D. D. B., & Abbot, D. S. 2016, *The Astrophysical Journal*, 825, 99
- Kopparapu, R. K., Wolf, E. T., Arney, G., Batalha, N. E., Haqq-Misra, J., Grimm, S. L., & Heng, K. 2017, *The Astrophysical Journal*, 845, 5
- Kopparapu, R. K., Wolf, E. T., Haqq-Misra, J., Yang, J., Kasting, J. F., Meadows, V., Terrien, R., & Mahadevan, S. 2016, *The Astrophysical Journal*, 819, 84
- Kopparapu, R. K., et al. 2013, *The Astrophysical Journal*, 765, 131
- Kuang, Z., & Hartmann, D. L. 2007, *Journal of Climate*, 20, 2051, DOI: 10.1175/JCLI4124.1
- Lecante, J., Forget, F., Charnay, B., Wordsworth, R., & Pottier, A. 2013a, *Nature*, 504, 268
- Lecante, J., Forget, F., Charnay, B., Wordsworth, R., Selsis, F., Millour, E., & Spiga, A. 2013b, *Astronomy And Astrophysics*, 554, A69
- Lewis, N. T., Lambert, F. H., Boutle, I. A., Mayne, N. J., Manners, J., & Acreman, D. M. 2018, *The Astrophysical Journal*, 854, 1
- Manabe, S., & Wetherald, R. 1967, *Journal of the Atmospheric Sciences*, 24, 241
- Merlis, T. M., & Schneider, T. 2010, *Journal of Advances in Modeling Earth Systems*, 2
- Neale, R. B., et al. 2010, *Description of the NCAR Community Atmosphere Model (CAM 4.0)*, http://www.cesm.ucar.edu/models/ccsm4.0/cam/docs/description/cam4_desc.pdf
- Pierrehumbert, R. T. 1995, *Journal of the Atmospheric Sciences*, 52, 1784
- . 2010, *Principles of Planetary Climate* (Cambridge University Press)
- . 2011, *Astrophys J. Lett.*, 726, L8, doi:10.1088/2041-8205/726/1/L8

- Pierrehumbert, R. T., Brogniez, H., & Roca, R. 2007, On the relative humidity of the Earth's atmosphere
- Pierrehumbert, R. T., & Ding, F. 2016, *Proceedings of the Royal Society A*, 2190, 136, doi:10.1098/rspa.2016.0107
- Popp, M., Schmidt, H., & Marotzke, J. 2016, *Nature Communications*, 7, 10627
- Romps, D., & Kuang, Z. 2009, *GRL*, 36, L09804, doi:10.1029/2009GL037396
- Salameh, J., Popp, M., & Marotzke, J. 2017, *Climate Dynamics*, 1
- Sherwood, S. C., Roca, R., Weckwerth, T. M., & Andronova, N. G. 2010, *Reviews of Geophysics*, 48, 1
- Shields, A. L., Bitz, C. M., Meadows, V. S., Joshi, M. M., & Robinson, T. D. 2014, *The Astrophysical Journal Letters*, 785, L9
- Shields, A. L., Meadows, V. S., Bitz, C. M., Pierrehumbert, R. T., Joshi, M. M., & Robinson, T. D. 2013, *Astrobiology*, 13, 715
- Thompson, D. W. J., Bony, S., & Li, Y. 2016, *PNAS*, 114(31), 8181, <https://doi.org/10.1073/pnas.1620493114>
- Turbet, M., Leconte, J., Selsis, F., Bolmont, E., Forget, F., Ribas, I., Raymond, S. N., & Anglada-Escudé, G. 2016, *Astronomy & Astrophysics*, 596, A112
- Turbet, M., et al. 2018, *Astronomy & Astrophysics*, 612, 22
- Vallis, G. K. 2017, *Atmospheric and Oceanic Fluid Dynamics: Fundamentals and Large-Scale Circulation* (Cambridge, U.K.: Cambridge University Press), 964
- Vallis, G. K., et al. 2018, *Geoscientific Model Development*, 11, 843
- Wallace, J. M., & Hobbs, P. V. 2016, *Atmospheric Science: An Introductory Survey* (Cambridge, U.K.: Academic Press), 504
- Wang, Y., Feng, T., & Hu, Y. 2014, *ApJ*, 791, L12, doi:10.1088/2041-8205/791/1/L12
- Wang, Y., Liu, Y., Feng, T., Yang, J., Ding, F., Zhou, L., & Hu, Y. 2016, *ApJ*, 823, L20, doi:10.3847/2041-8205/823/1/L20
- Way, M., Del Genio, A., Kelley, M., Aleinov, I., & Clune, T. 2015, arXiv preprint arXiv:1511.07283

- Way, M. J., et al. 2017, *The Astrophysical Journal Supplement Series*, 231, 12
- Wolf, E., & Toon, O. 2014, *Geophysical Research Letters*, 41, 167172, doi:10.1002/2013GL058376
- . 2015, *JGR*, 120, 5775
- Wolf, E. T. 2017, *The Astrophysical Journal Letters*, 839, L1
- Wolf, E. T., Shields, A. L., Kopparapu, R. K., Haqq-Misra, J., & Toon, O. B. 2017, *The Astrophysical Journal*, 837, 107
- Wordsworth, R., Forget, F., & Eymet, V. 2010a, *Icarus*, 210, 992
- Wordsworth, R., Forget, F., Selsis, F., Madeleine, J.-B., Millour, E., & Eymet, V. 2010b, *Astronomy & Astrophysics*, 522, A22
- Wordsworth, R. D., Forget, F., Selsis, F., Millour, E., Charnay, B., & Madeleine, J.-B. 2011, *Astrophys. J. Lett.*, 733, L48, doi:10.1088/2041-8205/733/2/L48
- Wordworth, R. 2015, *The Astrophysical Journal*, 808, 1
- Wright, J. S., Sobel, A., & Galewsky, J. 2010, *Journal of Climate*, 23, 4556
- Yang, J., & Abbot, D. S. 2014, *Astrophysical Journal*, 784, 155, doi:10.1088/0004-637X/784/2/155
- Yang, J., Boué, G., Fabrycky, D. C., & Abbot, D. S. 2014, *Astrophysical Journal Letters*, 787, L2, doi:10.1088/2041-8205/787/1/L2
- Yang, J., Cowan, N. B., & Abbot, D. S. 2013, *Astrophysical Journal Letters*, 771, L45, DOI:10.1088/2041-8205/771/2/L45
- Yang, J., et al. 2016, *The Astrophysical Journal*, 826, 222